Observation of giant interfacial spin Hall angle in $Y_3Fe_5O_{12}$/Pt heterostructures

Y. Dai,[1] S. J. Xu,[1] S. W. Chen,[1] X. L. Fan,[2] D. Z. Yang,[2] D. S. Xue,[2] D. S. Song,[3] J. Zhu,[3] S. M. Zhou,[1] and Xuepeng Qiu[1,*]

[1]*Shanghai Key Laboratory of Special Artificial Microstructure Materials and Technology, and Pohl Institute of Solid State Physics, School of Physics Science and Engineering, Tongji University, Shanghai 200092, China*

[2]*The Key Lab for Magnetism and Magnetic Materials of Ministry of Education, Lanzhou University, Lanzhou 730000, China*

[3]*National Center for Electron Microscopy in Beijing, Key Laboratory of Advanced Materials (MOE), and The State Key Laboratory of New Ceramics and Fine Processing, School of Materials Science and Engineering, Tsinghua University, Beijing 100084, China*

(Received 2 April 2019; revised manuscript received 23 July 2019; published 9 August 2019)

By self-consistently resolving the disentanglement of the spin Hall angle (SHA) and the spin diffusion length (SDL) through the ratio of Hanle and spin Hall magnetoresistances, the SHA in heavy metals has been for the first time rigorously extracted. For Pt on ferromagnetic insulator $Y_3Fe_5O_{12}$, the genuine SHA scales as an exponential function of the Pt layer thickness. The spin Hall effect is proved to be dominated by the Berry-phase-induced intrinsic mechanism. In particular, the giant interfacial SHA of 0.33 is observed and is attributed to the broken-symmetry-induced nonspecular electronic scattering at the $Y_3Fe_5O_{12}$/Pt interface. At last, the spin relaxation process is found to be dominated by the Elliott-Yafet and D'yakonov-Perel' mechanisms for thin and thick Pt layers, respectively.

DOI: 10.1103/PhysRevB.100.064404

I. INTRODUCTION

With great prospects for new generation of information storage, spin current devices have attracted immense attention because Joule heat can be avoided during operation [1–3]. The performance of spin current devices is governed by the generation and the propagation of pure spin current [4]. Arising from the spin Hall effect (SHE), the spin current generation is determined by the spin Hall angle (SHA) of heavy metals (HMs). Meanwhile, the propagation of the spin current is governed by the spin diffusion length (SDL) of HMs. Therefore, the SHA and the SDL are two critical parameters to control the pure-spin-current-related phenomena, such as spin Hall magnetoresistance (SMR) [5,6], Hanle magnetoresistance (HMR) [7,8], spin pumping [9,10], and spin transfer torque-ferromagnetic resonance [11].

Recently, the interfacial SHA has been theoretically predicted to be about 2 orders larger than the bulk one [12], providing an encouraging route to enhance the spin-charge conversion efficiency. However, the direct characterization of interfacial SHA has still been rare in experiments. In order to reveal the nature of interfacial SHA, it is essential to study the SHE scaling law. The SHA is theoretically predicted to obey the following linear scaling law [4,13]:

$$\theta_{\mathrm{SH}} = a + b\rho_{xx}, \tag{1}$$

where ρ_{xx} is the sheet resistivity of the HM layers, a refers to the SHA contributed by the spin skew scattering process, and b corresponds to the scattering-independent spin Hall conductivity (SHC) contributed by the intrinsic and extrinsic side-jump terms. While the intrinsic term is caused by the spin-orbit coupling (SOC)-induced Berry phase in k space [14,15], the extrinsic skew scattering and side-jump terms are related to the interaction between the disorder scattering and the SOC [16–18]. However, up to now, there still have been very few experimental advances to rigorously show the scaling law in Eq. (1). The difficulty underlying above critical issues is due to the fact that the SHA and the SDL are perpetually entangled with each other in spin-current-related phenomena [5,6,9–11]. For simplicity, most experimental studies start out with the assumption that the SHA and the SDL are both independent of the HM layer thickness.

In the present work, we first examine the SMR in $Y_3Fe_5O_{12}$ (YIG)/Pt heterostructures to point out that the above assumption of invariant SHA and SDL in the conventional approach is oversimplified. Accordingly, we develop an innovative approach to disentangle and extract the genuine SHA and SDL of Pt through SMR and HMR [7,8]. It is found that the SHA changes as an exponential function of the Pt layer thickness. The interfacial SHA in YIG/Pt heterostructures is observed to be as large as 0.33, about five times larger than the bulk SHA of 0.07. Moreover, studies of scaling laws show the dominance of the intrinsic SHE in the present YIG/Pt system. Last, we elucidate the mechanism of the spin relaxation process.

II. SAMPLE FABRICATION AND MEASUREMENTS

A series of high quality $Y_3Fe_5O_{12}$ (YIG, 50 nm)/Pt heterostructures with different Pt layer thicknesses was prepared. YIG layers were first fabricated on (111) $Gd_3Ga_5O_{12}$ (GGG)

*xpqiu@tongji.edu.cn

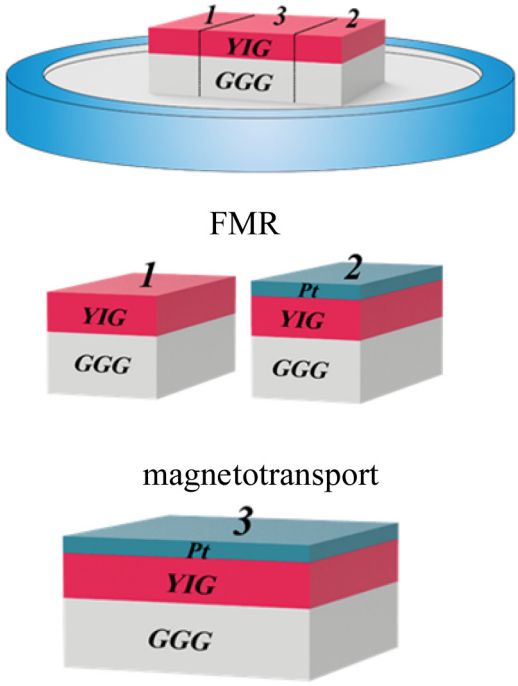

FIG. 1. Schematic diagram of sample preparation. GGG substrate was placed in the central location of the sample tray which was kept rotating around its center during deposition (top). The symmetrically located small pieces 1 and 2 were prepared for ferromagnetic resonance (FMR) measurements to minimize sample variation (center). Piece 3 was used for magnetotransport measurements (bottom).

substrates with an area of 1.0 cm × 0.80 cm from a stoichiometric polycrystalline target by pulsed laser deposition (PLD) at 625 °C. Post annealing was performed at 810 °C for 4 h to promote epitaxial growth of YIG. The base pressure of the PLD cavity was better than 2×10^{-6} Pa and the growth rate of YIG was 0.33 Å/s. In order to avoid the run-to-run error, each large YIG sample was then cut into three small pieces, as shown in Fig. 1 . The Pt layer was then deposited on small pieces 2 and 3 at ambient temperature by DC magnetron sputtering, where the base pressure of the sputtering system was greater than 2×10^{-6} Pa and the Ar pressure was 0.4 Pa during deposition. The deposition rate of Pt was 0.68 Å/s. Here, small pieces 1 and 2 were used for ferromagnetic resonance (FMR) measurements of YIG single layers and YIG/Pt heterostructures, respectively, and small piece 3 was used for magnetic transport measurements of YIG/Pt heterostructures. The film thickness and microstructure were characterized at room temperature by x-ray reflection (XRR) and x-ray diffraction (XRD), respectively, using a D8 Discover x-ray diffractometer with Cu Kα radiation. The XRD results in Figs. 2(a)–2(c) prove the epitaxial growth of the YIG (111) layer on the GGG (111) substrate, which is further confirmed by the high-resolution transmission electron microscope (HRTEM) and the selected area electron diffraction (SAED) patterns in Figs. 2(d) and 2(e). Moreover, the magnetization of the YIG layer measured by a vibrating sample magnetometer was determined to be 150 emu/cm^3. Measurements of SMR and HMR were performed in the physical properties measurement system. The gyromagnetic ratio of the YIG

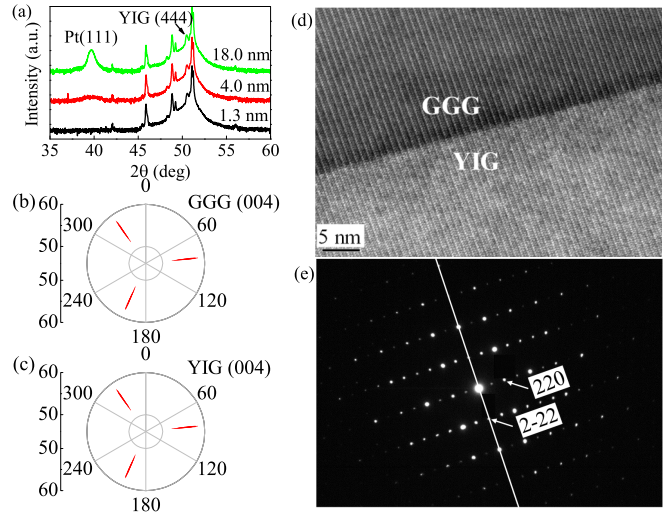

FIG. 2. XRD of YIG/Pt bilayers (a). Pole figures of GGG (b) and YIG (c). The HRTEM (d) and the SAED (e) patterns of YIG. Here, all the measurements were made at room temperature.

layer and the spin mixing conductance (SMC) at the YIG/Pt interface were measured by FMR technique with a coplanar waveguide [19].

III. RESULTS AND DISCUSSION

FMR derivative spectra of YIG and YIG/Pt samples were measured in the frequency (f) range from 4 to 18 GHz with the aid of a coplanar waveguide. Typical spectra of YIG and YIG/Pt in Fig. 3(a) were fitted by Lorentzian function to obtain the resonance field and the peak-to-peak linewidth ΔH_{pp}. By fitting the measured dispersion relation with the Kittel equation [20], as shown in Fig. 3(b), the gyromagnetic ratio γ of YIG and YIG/Pt was obtained to be 17.88 and 17.87 GHz/kOe, respectively. According to the relation $\gamma = \frac{\mu_0 |e|}{2m} g$, the Landé factor $g \approx 2.0$. Next, the full-width at half maximum (FWHM) linewidth ΔH was obtained by $\Delta H = \sqrt{3}\Delta H_{pp}$. For YIG and YIG/Pt, ΔH changes as a function of f, as shown in Fig. 3(c). The Gilbert damping parameter α of YIG and YIG/Pt was determined to be 5.6×10^{-4} and 1.78×10^{-3} by the equation $\Delta H = \Delta H_0 + \frac{4\pi\alpha}{\gamma} f$, where ΔH_0 arises from the inhomogeneity of the YIG layer [21].

The real part G_r of the SMC at the YIG/Pt interface in Fig. 3(d) is directly determined experimentally by the following equation [22]:

$$G_r = \frac{4\pi M_s t_{\mathrm{YIG}}}{g\mu_B}(\alpha_{\mathrm{YIG/Pt}} - \alpha_{\mathrm{YIG}}), \tag{2}$$

where the YIG layer thickness $t = 50$ nm, the YIG saturation magnetization $M_S = 150$ emu/cm^3, α_{YIG} and $\alpha_{\mathrm{YIG/Pt}}$ are the magnetic damping factors of the YIG layer and the YIG/Pt heterostructure, respectively. The drop of G_r at large d can be related to smaller interface roughness or weak interdiffusion for thick Pt layers. As demonstrated in the inset of Fig. 3(d), the root mean square (RMS) roughness at the YIG/Pt interface, fitted from the XRR spectra of YIG/Pt, decreases with increasing d, indicating a smoother YIG/Pt interface for large d.

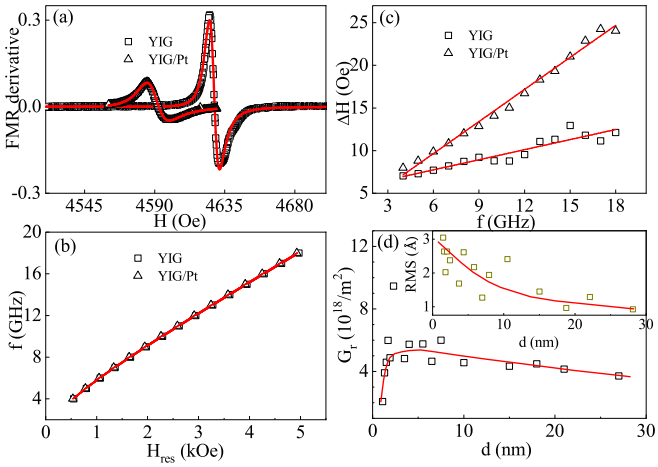

FIG. 3. For YIG and YIG/Pt, FMR derivative spectra at the frequency $f = 17$ GHz (a), FMR dispersion (b), and the FWHM linewidth versus the frequency (c). The real part of the SMC in YIG/Pt is shown in panel (d). In panels (a)–(c), the Pt layer is 4.0 nm thick and solid lines refer to the fitted results. In panel (d), solid lines serve as a guide to the eye. The inset of panel (d) shows the RMS roughness at the YIG/Pt interface, as fitted from the XRR spectra at small angles. Measurements of FMR were measured at $T = 200$ K, and the XRR in the inset of panel (d) was measured at $T = 300$ K.

Basic features of SMR and HMR are summarized in Fig. 4. In SMR [5,6], due to the SHE in the Pt layer, the spin current is produced in the direction perpendicular to the charge current J_c. Since the reflected spin current at the Pt/YIG interface is modified by the YIG magnetization, the additional charge current J_C' is produced in the Pt layer due to the inverse SHE, as schematically shown in Fig. 4(a). Accordingly, SMR

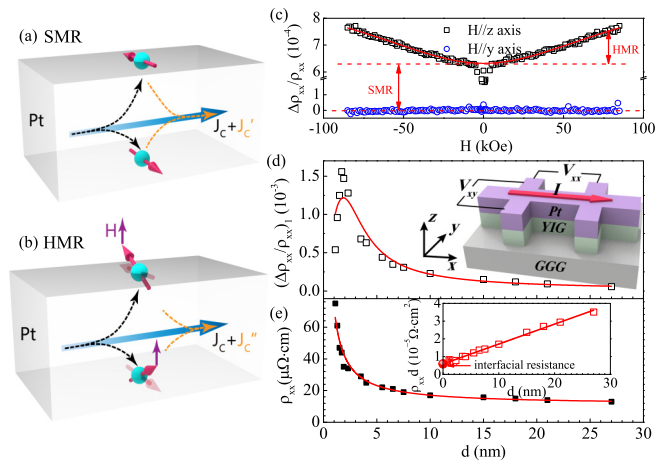

FIG. 4. Schematic pictures of SMR (a) and HMR (b) mechanisms. For YIG (50 nm)/Pt (4.0 nm), the magnetoresistance ratio $\Delta\rho_{xx}/\rho_{xx}$ versus the external magnetic field H along the y axis and the z axis (c). SMR in YIG/Pt (d) and sheet resistivity in single Pt layers (e) as a function of the Pt layer thickness d. The inset in panel (d) shows the schematic picture of SMR and HMR measurements. The inset in panel (e) shows the film thickness dependence of the product of the sheet resistivity and the film thickness. In panels (c), (d), and (e), solid lines refer to the fitted results and $T = 200$ K.

manifests itself as the change of sheet resistivity when the YIG magnetization is rotated in the yz plane. The total sheet resistivity of YIG/Pt obeys the following equation, $\rho_{xxt} = \rho_{xx} + \Delta\rho_{xx}(1 - m_y^2)$, where m_y is the component of the YIG magnetization unit vector along the y axis, ρ_{xx} is the sheet resistivity of single Pt layers, and $\Delta\rho_{xx}$ is the magnitude of the changed sheet resistivity in YIG/Pt when the YIG magnetization is rotated from the y axis to the z axis. In HMR [7,8], spin precession around the external magnetic field H leads to dephasing of electron spins, as shown in Fig. 4(b), which subsequently leads to the modification of the SDL [7,8]. Therefore, the reflected spin current density, the additional charge current density J_C'', and the total sheet resistivity all depend on the magnitude and the orientation of the external magnetic field in HMR. SMR and HMR ratios near zero external magnetic field H and at high H are defined in Fig. 4(c). The SMR of YIG/Pt maximizes around the Pt layer thickness $d = 1.9$ nm, as shown in Fig. 4(d), and it obeys the following equation [5,6]:

$$(\Delta\rho_{xx}/\rho_{xx})_1 \approx \frac{\theta_{\rm SH}^2\lambda_{\rm sd}}{d}\frac{\tanh^2(d/2\lambda_{\rm sd})}{1/(2\rho_{xx}\lambda_{\rm sd}G_r)+\coth(d/\lambda_{\rm sd})}, \quad (3)$$

where $\theta_{\rm SH}$, $\lambda_{\rm sd}$, d, and G_r are the SHA, the SDL, the Pt layer thickness, and the real part of the SMC at the YIG/Pt interface, respectively. With the assumption that both the SHA and the SDL are invariant with Pt thickness and by adopting the experimentally acquired sheet resistivity [Fig. 4(e)] and the real part of SMC, the fit in Fig. 4(d) with Eq. (3) gives an SHA of 0.195 and an SDL of 0.96 nm. Although the overall variation trend of the SMR in Fig. 4(d) seems to be fitted, with a closer look, we see that a big discrepancy between fitted and measured results exists for $d < 3.5$ nm, in particular near $d = 1.9$ nm. As discussed below, the HMR/SMR ratio versus H curves for most of the YIG/Pt samples *cannot* be fitted *at all* with the SDL of 0.96 nm. These observations clearly indicate that a set of fixed SDL and SHA cannot satisfactorily explain spin transport at different Pt thicknesses. Instead, both the SDL and the SHA should depend on the Pt layer thickness.

Moreover, the product of the sheet resistivity ρ_{xx} and the film thickness d is observed to change linearly with the film thickness, as shown in the inset of Fig. 4(e). Since the product is found to well obey the equation $\rho_{xx}d = \rho_{xxb}d + \rho_{xxs}$ with the bulk resistivity ρ_{xxb} and the interfacial resistivity ρ_{xxs}, the nonspecular reflection of electrons at the interface/surface is identified through quantifying ρ_{xxs}. The bulk resistivity ρ_{xxb} and the interfacial resistivity ρ_{xxs} are fitted to be 11.0 $\mu\Omega$ cm and 58.0 $\mu\Omega\,{\rm cm}^2$, respectively. The bulk resistivity is close to the value of 10.0 $\mu\Omega$ cm in bulk Pt [23] whereas the large interfacial resistivity is caused by the ideal morphology at the YIG/Pt interface, as demonstrated by the small interface roughness in the inset of Fig. 3(d).

The HMR at high magnetic fields can be rigorously described by the following equation [7]:

$$(\Delta\rho_{xx}/\rho_{xx})_2 \approx {\rm Re}\left\{\frac{\theta_{\rm SH}^2\Lambda_{\rm sd}}{d}\frac{\tanh^2(d/2\Lambda_{\rm sd})}{1/(2\rho_{xx}\Lambda_{\rm sd}G_r)+\coth(d/\Lambda_{\rm sd})}\right\} - \left\{\frac{\theta_{\rm SH}^2\lambda_{\rm sd}}{d}\frac{\tanh^2(d/2\lambda_{\rm sd})}{1/(2\rho_{xx}\lambda_{\rm sd}G_r)+\coth(d/\lambda_{\rm sd})}\right\}, \quad (4)$$

where the first and the second terms on the right-hand side refer to the SMR at high magnetic fields and zero magnetic field, respectively. The approximations in Eqs. (3) and (4) are made by assuming that the imaginary part of the SMC is much smaller than the real part [5–7]. The effective SDL Λ_{sd} is modified by spin precession around the external magnetic field H through the equation $1/\Lambda_{sd} = \sqrt{1/\lambda_{sd}^2 + i/\lambda_m^2}$, with $\lambda_m = \sqrt{D\hbar/g\mu_B B}$, where g, μ_B, D, and B are the Landé factor, the Bohr magneton, the electron diffusion coefficient (EDC), and the magnetic induction intensity, respectively, and $i^2 = -1$. The HMR will vanish when $\Lambda_{sd} = \lambda_{sd}$ at $H = 0$. Most remarkably, the HMR/SMR ratio is independent of the SHA and thus the SHA and the SDL can be easily disentangled. The HMR/SMR ratio reads

$$\mathrm{HMR/SMR} = \mathrm{Re}\left\{\frac{1}{\sqrt{1+\frac{i\lambda_{sd}^2 g\mu_B B}{D\hbar}}}\frac{\tanh^2\left(\frac{d\sqrt{\frac{1}{\lambda_{sd}^2}+\frac{ig\mu_B B}{D\hbar}}}{2}\right)}{\tanh^2\left(\frac{d}{2\lambda_{sd}}\right)}\frac{1+2\lambda_{sd}\rho_{xx}G_r\coth\left(\frac{d}{\lambda_{sd}}\right)}{1+\frac{2\rho_{xx}G_r\coth\left(d\sqrt{\frac{1}{\lambda_{sd}^2}+\frac{ig\mu_B B}{D\hbar}}\right)}{\sqrt{\frac{1}{\lambda_{sd}^2}+\frac{ig\mu_B B}{D\hbar}}}}\right\} - 1. \quad (5)$$

After removing the entanglement of the SHA and the SDL, the values of the SDL and the EDC can be obtained by fitting the HMR/SMR ratio as a function of the magnetic field H. For the HMR curve of YIG/Pt (4.0 nm) heterostructures in Fig. 4(c), the SDL and the EDC are fitted to be 4.50 nm and 2.28×10^{-5} m^2/s, respectively, where the sheet resistivity $\rho_{xx} = 25.0\ \mu\Omega\,\mathrm{cm}$, $G_r = 5.74 \times 10^{18}\,\mathrm{m}^{-2}$, and the Landé factor $g \approx 2.0$. With the data of the SDL and the SMR, the SHA of YIG/Pt (4.0 nm) is derived to be 0.105 from Eqs. (3) and (5). In particular, with the strict HMR expression in Eq. (4), *only one set* of the SDL and the EDC can be self-consistently extracted. As shown in Fig. 5, if one assigns the SDL and the EDC with other values that deviate from 4.50 nm and 2.28×10^{-5} m^2/s, the fitted results cannot reproduce the measured results of $d = 4.0$ nm. Subsequently, the methodology based on Eq. (5) has been employed for all other samples to rigorously acquire the EDC and the SDL. As mentioned earlier, here we note that, with the SDL of 0.96 nm, the HMR/SMR of most samples cannot be fitted at all even with a variety of the EDC, as shown by typical results of $d = 1.1$ nm in Fig. 6. Therefore, the conventional assumption that the SDL and the SHA are independent of Pt thickness is further proved to be oversimplified.

As the HMR and the SMR both become very small and the measurement noise becomes significant for thick Pt

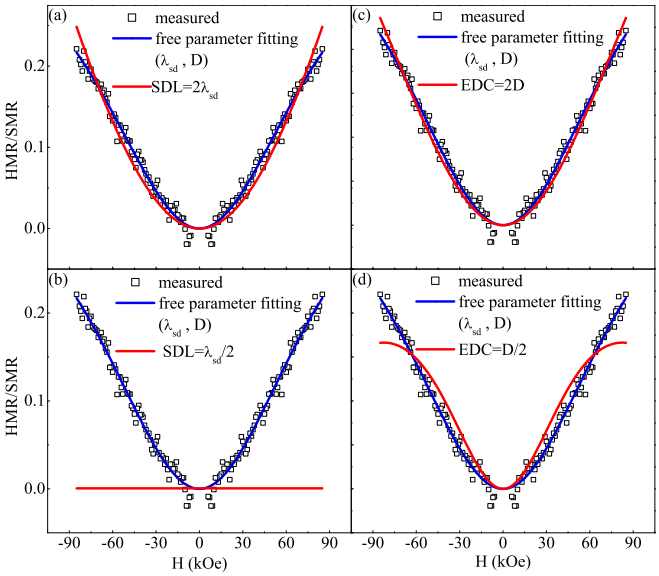

FIG. 5. For YIG/Pt (4.0 nm), measured HMR/SMR ratio versus H curve (open boxes) is shown in panels (a)–(d). The blue lines in panels (a)–(d) refer to the fitted results where the SDL and the EDC are fitted to be 4.50 nm and 2.28×10^{-5} m^2/s as free parameters, respectively. The red lines refer to the fitted results with the SDL = 8.86 nm (a) and 2.20 nm (b) and the EDC as a free parameter (a, b), and with the EDC = 4.5×10^{-5} m^2/s (c) and 1.1×10^{-5} m^2/s (d) and the SDL as a free parameter (c, d). Measurements of HMR and SMR were performed at $T = 200$ K.

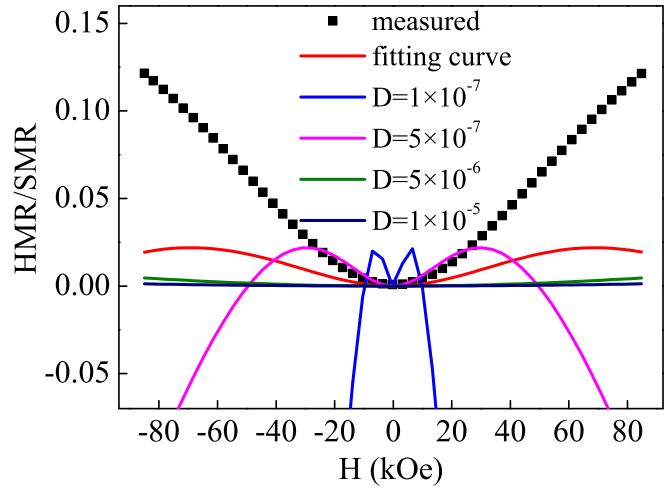

FIG. 6. For YIG/Pt (1.1 nm), measured HMR/SMR ratio versus H (black boxes) is shown. In all fitted and calculated results (solid lines), the SDL is always fixed to be 0.96 nm, which is fitted from the results in Fig. 4(d) through Eq. (3), under the conventional assumption that the SDL and the SHA are independent of the Pt layer thickness. As a free parameter, the EDC is fitted to be 1.2×10^{-6} m^2/s, as shown by the red line. Calculations were made with other values of the EDC, as shown by solid lines of other colors. All fitted results and calculations deviate from the experimental results. Measurements of HMR and SMR were performed at $T = 200$ K. Therefore, the SDL of $d = 1.1$ nm is not 0.96 nm at $T = 200$ K.

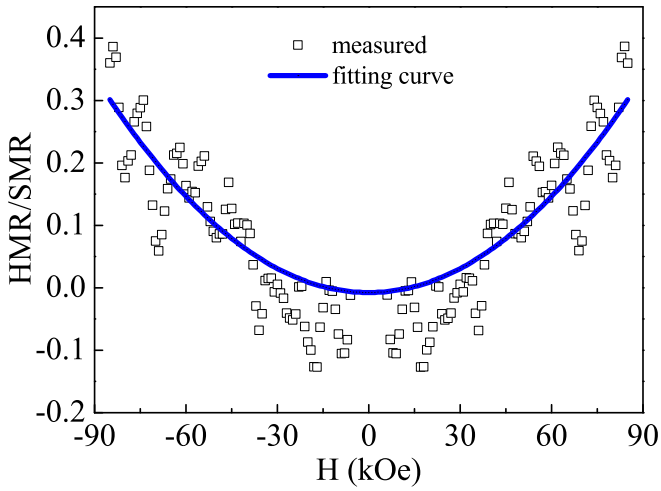

FIG. 7. The measured HMR/SMR ratio (open box) of YIG/Pt (18.0 nm) is fitted with the SDL and the EDC as free parameters. Due to large measurement noise, the SDL and the EDC are fitted to be as large as 282 nm and 0.16 m^2/s, respectively. Measurements of HMR and SMR were performed at $T = 200$ K.

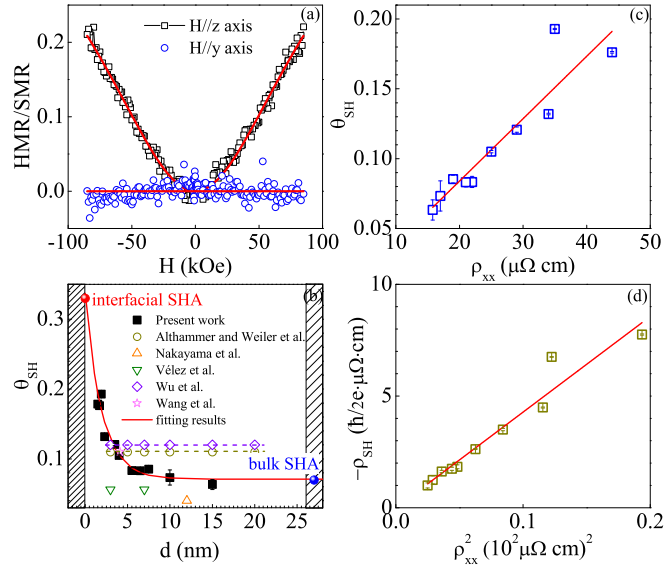

FIG. 8. The HMR/SMR ratio of YIG/Pt (4.0 nm) (a), SHA versus Pt layer thickness (b), SHA θ_{SH} versus ρ_{xx} (c), and spin Hall resistivity ρ_{SH} versus ρ_{xx}^2 (d). In panels (a)–(d), solid lines refer to the fitted results. In panel (b), interfacial and bulk SHAs are extracted, and the data of the SHA in other research groups are given for comparison, including Refs. [5,30] (dark yellow, circles), [6] (orange, up triangle), [7] (olive, down triangle), [8] (violet, diamond), and [29] (light magenta, five-pointed star). In panel (d), the spin Hall resistivity was obtained with the measured SHA in panel (c) and the sheet resistivity in Fig. 4(e) through the following equation: $\rho_{SH} = -\theta_{SH}\rho_{xx}\hbar/2e$. Measurements of HMR, SMR, SHA, and sheet resistivity were performed at $T = 200$ K.

samples, the SDL and the SHA cannot be fitted well. For $d = 18.0$ nm, for example, the large measurement noise of the HMR/SMR leads to large errors of the SDL and the EDC, as shown in Fig. 7. Moreover, for $d < 1.5$ nm, other factors, such as Rashba effects and extrinsic mechanisms, complicate the SHE scaling law [13,24,25]. The following discussion mainly focuses on the samples with Pt layers thickness of $1.5 \leqslant d \leqslant 15.0$ (nm).

In comparison, the data of Fig. 4(c) are replotted as the HMR/SMR ratio versus the external magnetic field, as shown in Fig. 8(a). Figure 8(b) shows that the genuine SHA changes significantly with the Pt layer thickness, which is in sharp contrast to most of the previous studies that assume a constant SHA value [5,6,26–30]. The SHA can be well fitted by the exponential function $\theta_{SH} = 0.070 + 0.266e^{-d/1.95}$, confirming the theoretical prediction of Wang *et al.* [12]. The exponential decay of the SHA with the film thickness arises from the exponential decay of the spin current along the film depth [12]. The interfacial SHA is extrapolated from the results of large d. While θ_{SH} approaches the bulk value of 0.070 for thick Pt layers, the interfacial SHA is as large as 0.33 when d approaches zero. The interfacial SHA is about five times larger than the bulk one. The large interfacial SHA arises from the Berry-phase-induced intrinsic mechanism, in addition to other possible mechanisms such as the Rashba effect and extrinsic mechanisms [13,24,25].

In order to elucidate the mechanism behind the giant interfacial SHA, it is essential to study the SHE scaling law. Notably, the SHA and the sheet resistivity show similar variation trends in Figs. 8(b) and 4(e). Consequently, the SHA in YIG/Pt is found to exhibit the linear scaling law of Eq. (1), as shown in Fig. 8(c). The scattering-independent parameter b is determined to be 4426 S/cm while the skew scattering parameter a is as small as -0.0071. In order to further separate the intrinsic contribution and the side-jump contribution, the empirical quadratic scaling law proposed by Tian *et al.* [13,24] is employed. Assuming that the contribution from the phonon-induced skew scattering can be neglected, the spin Hall resistivity changes as a quadratic function of ρ_{xx}, i.e,

$$\rho_{SH} = a' + b'\rho_{xx}^2, \tag{6}$$

with parameters a' and b' corresponding to the extrinsic spin Hall resistivity at zero temperature and the intrinsic SHC σ_{SH}^{int}, respectively. With the entire SHC $\sigma_{SH} = -\rho_{SH}/\rho_{xx}^2$, it obeys the following equations:

$$\sigma_{SH} = -a'\sigma_{xx}^2 - b', \tag{7}$$

$$\sigma_{SH}^{int} = -b', \tag{8}$$

where the electric conductivity $\sigma_{xx} = 1/\rho_{xx}$. Remarkably, Fig. 8(d) shows $-\rho_{SH} \propto \rho_{xx}^2$, $a' \approx 0$, and $\sigma_{SH}^{int} = -b' = 4280 \pm 370$ $(\hbar/2e)$S/cm. It is interesting to find that the measured value of the intrinsic SHC is close to the theoretical prediction of 4000 $(\hbar/2e)$S/cm [14]. As a result, the intrinsic SHC in the present YIG/Pt is expected to exhibit a weak temperature dependence for $T \leqslant 200$ K, different from the earlier *ab initio* calculations [14].

With Eq. (1) and the relation [13,31–33] $\sigma_{SH} = \theta_{SH}\sigma_{xx}\hbar/2e$, the entire SHC also reads as follows:

$$\sigma_{SH} = (a\sigma_{xx} + b)\hbar/2e, \tag{9}$$

$$b\hbar/2e = \sigma_{SH}^{int} + \sigma_{AH}^{sj}, \tag{10}$$

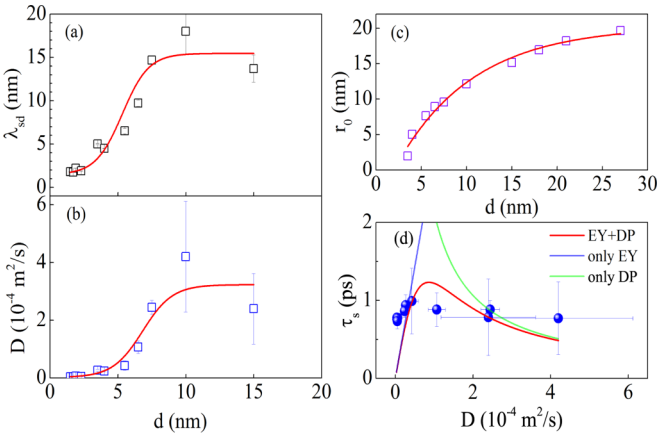

FIG. 9. Dependencies of the SDL λ_{sd} (a), the EDC D (b), and the grain size r_0 (c) on the Pt layer thickness. The spin relaxation time τ_s versus the EDC D (d). Solid lines serve a guide to the eye in panels (a) and (b) and refer to the fitted results in panels (c) and (d). In panel (c), measured data of the grain size can be fitted by an exponential function. In panel (d), the spin relaxation times contributed by the EY (blue line) and the DP (green line) models are also given for comparison. Here, $T = 200$ K.

where $b\hbar/2e$ is the scattering-independent SHC and σ_{AH}^{sj} is the side-jump SHC. Accordingly, with $b\hbar/2e = 4426\,\hbar/2e \cdot$ S/cm and $\sigma_{SH}^{int} = 4280 \pm 370\ \hbar/2e \cdot$ S/cm, σ_{AH}^{sj} is more than 1 order in magnitude smaller than σ_{SH}^{int}, i.e., $\sigma_{AH}^{sj} \approx 0$. This can be further verified with the relations [13,24]

$$a' = a''\rho_{xx0} + \beta\rho_{xx0}^2, \tag{11}$$

$$a'' = -a\hbar/2e, \tag{12}$$

$$\beta = -\sigma_{SH}^{sj}, \tag{13}$$

where ρ_{xx0} is the residual resistivity. Since a' and a are both negligible, as shown in Figs. 8(c) and 8(d), we have $\sigma_{SH}^{sj} = -\beta \approx 0$. In conclusion, the SHE in the present YIG/Pt is verified to be dominated by the Berry-phase-induced intrinsic mechanism. Subsequently, the giant interfacial SHA can be easily understood in terms of the interfacial resistivity and the intrinsic SHE. Finally, these two SHE scaling laws are both proven to be valid in the present Pt layers. It is noted that the skew scattering, the side-jump, and the intrinsic terms can be separated from each other only with both of these two scaling laws.

Figure 9 summarizes the results of the SDL, the EDC, and the grain size of Pt layers r_0. Here, the grain size is estimated from the FWHM line broadening $\Delta\theta$ of the XRD peak through the Scherrer equation [34] $r_0 = K\lambda/\Delta\theta\cos\theta$, where K is a dimensionless shape factor with a value close to unity, λ is the x-ray wavelength, and θ is the Bragg angle. It is interesting to find that the SDL, the EDC, and the grain size all increase and approach saturation for thick Pt layers, as shown in Figs. 9(a)–9(c). The grain size changes as an exponential function of the film thickness, as shown in Fig. 9(c). For the nanometer-thick Pt layers in spintrionics devices, the mean free path λ_e is close to or larger than the Pt layer thickness and the grain size [27]. Due to the finite size effect, the EDC D ($= \lambda_e v_F$, with v_F being the Fermi velocity) shows a variation trend close to the grain size as a function of the film thickness, as shown in Figs. 9(b) and 9(c). The observable difference between the EDC and the grain size in Figs. 9(b) and 9(c) arises from additional electron scattering events from the interface/surface.

Self-consistent extraction of the EDC and the SDL allows us to further reveal the quantitative relation between the spin relaxation time τ_s and the electron relaxation time τ_e. In the spin transport model [35], the SDL $\lambda_{sd} = \sqrt{D\tau_s}$. With the data of the SDL and the EDC in Figs. 9(a) and 9(b), the spin relaxation time τ_s is obtained [Fig. 9(d)], which can be utilized to discuss the spin relaxation mechanism. In EY [36,37] and DP [38–40] spin relaxations, τ_s is proportional and inversely proportional to τ_e, respectively. By considering both the EY and the DP processes and knowing the EDC $D = v_F^2\tau_e$, the entire spin flip rate $1/\tau_s = \alpha/D + \langle\Omega_k^2\rangle D$, where the parameter α is proportional to ξ^2 with the bulk SOC strength ξ in the perturbation theory, and $\langle\Omega_k^2\rangle$ is proportional to the average precession frequency around the SOC-induced effective magnetic field. The nonmonotonic variation of τ_s with the EDC in Fig. 9(d) thus clearly indicates contributions of both the EY and the DP models. Parameters α and $\langle\Omega_k^2\rangle$ are fitted to be 3.5×10^7 m^2/s^2 and 4.7×10^{15} m^{-2}, respectively. For d smaller (larger) than 7.5 nm, the spin relaxation process is dominated by the EY (DP) model [26,41]. Moreover, the measured data cannot be fitted at all with only either the EY or the DP model, as shown in Fig. 9(d).

The present methology of rigorous determinations of both the SDL and the SHA is of great importance for spintronics research. Since the ratio of the interfacial and the bulk SHAs is close to that of the interfacial and the bulk resistivities, in the region of 5.0 ± 0.3, in good agreement with the SHE proportional scaling law, the giant interfacial SHA is further proved to arise from the large interfacial resistivity that is caused by the broken-symmetry-induced electronic scattering at the YIG/Pt interface. Thus, the physical source of the interfacial SHA is different from the Rashba effect in Pt/Cu metallic thin films [25]. The magnitude of the interfacial SHA in YIG/Pt is much larger than that of Co/Pt heterostructures [27] because of different electronic structures and magnetic proximity effects in insulating ferromagnet/Pt and metallic ferromagnet/Pt heterostructures [42,43]. With the dominance of the intrinsic mechanism, the sign of the SHA is determined by the Berry curvature of Pt instead of microstrucutres [4,14,15]. It is therefore well explained that the positive SHA is always observed experimentally despite a variety of microstructures in Pt layers [4,11,19,29]. In a similar way, the negative sign of the SHA in W and Ta, as shown in Table III of Ref. [4], can also be easily understood as an intrinsic material attribute. Moreover, the observed proportional dependence of the SHA on the sheet resistivity also one allows to solve the discrepancy of the SHA magnitude in Pt layers among various research groups by taking into account different sheet resistivities of the Pt layers [5–8,12,29]. It also helps to explain the alloying-induced enhancement of the SHA [19,44–46]. At last, the dependence of the SDL and the SHA on the HM layer thickness also facilitate the understanding of spin pumping results in ferromagnet/HM heterostructures [19,27].

It is noted that the HMR is advantageous over conventional electric approaches with respect to measurements of the EDC in polyvalent HM metals. Although the Hall coefficient of the HM metals can be measured directly, it is difficult to genuinely characterize the EDC due to the coexistence of electronlike and holelike carriers [26,41,47]. In contrast, with the HMR approach, the EDC can be self-consistently and rigorously determined by Eq. (5) with measured data of the sheet resistivity, the HMR/SMR ratio, the SMC, and the Landé g factor. For metallic ferromagnet/HM heterostructures, the HMR should be separated from the magnetoresistance of metallic ferromagnet layers in order to rigorously extract the SHA and the SDL of the HM layers.

In conclusion, we have for the first time self-consistently determined the SHA in Pt layers as a function of the Pt layer thickness after disentangling the SDL and the SHA through HMR and SMR. The SHA changes as an exponential function of the Pt layer thickness. The interfacial SHA is extrapolated to be as large as 0.33, about five times larger than the bulk value of 0.07. More importantly, the giant interfacial SHA is induced by the nonspecular electronic scattering at the interface with the broken symmetry because the SHC is dominated by the intrinsic mechanism. Since the spin relaxation time changes nonmonotonically with the electron relaxation time, the spin relaxation process is dominated by the EY model for thin Pt layers and by the DP model for thick Pt layers. The present work will provide a route to enhance the spin-charge conversion efficiency by controlling the insulating ferromagnet/HM interface morphology.

ACKNOWLEDGMENTS

This work was supported by the State Key Project of Fundamental Research under Grant No. 2015CB921501; the National Key R & D Program of China under Grants No. 2017YFA0305300 and No. 2017YFA0303202; the National Science Foundation of China under Grants No. 51331004, No. 51501131, No. 51671147, No. 11874283, No. 51801152, No. 11674246, and No. 11774064; the Natural Science Foundation of Shanghai under Grants No. 17ZR1443700 and No. 19ZR1478700; the Program for Professor of Special Appointment (Eastern scholar) at Shanghai Institutions of Higher Learning (Grant No. TP2016016) and the Fundamental Research Funds for the Central Universities.

Y.D. and S.J.X. contributed equally to this work.

[1] T. Jungwirth, J. Wunderlich, and K. Olejnik, Nat. Mater. **11**, 382 (2012).
[2] L. Liu, O. J. Lee, T. J. Gudmundsen, D. C. Ralph, and R. A. Buhrman, Phys. Rev. Lett. **109**, 096602 (2012).
[3] I. M. Miron, T. Moore, H. Szambolics, L. D. Buda-Prejbeanu, S. Auffret, B. Rodmacq, S. Pizzini, J. Vogel, M. Bonfim, A. Schuhl, and G. Gaudin, Nat. Mater. **10**, 419 (2011).
[4] J. Sinova, S. O. Valenzuela, J. Wunderlich, C. H. Back, and T. Jungwirth, Rev. Mod. Phys. **87**, 1213 (2015).
[5] M. Althammer, S. Meyer, H. Nakayama, M. Schreier, S. Altmannshofer, M. Weiler, H. Huebl, S. Geprägs, M. Opel, R. Gross, D. Meier, C. Klewe, T. Kuschel, J.-M. Schmalhorst, G. Reiss, L. Shen, A. Gupta, Y.-T. Chen, G. E. W. Bauer, E. Saitoh, and S. T. B. Goennenwein, Phys. Rev. B **87**, 224401 (2013).
[6] H. Nakayama, M. Althammer, Y. T. Chen, K. Uchida, Y. Kajiwara, D. Kikuchi, T. Ohtani, S. Geprägs, M. Opel, S. Takahashi, R. Gross, G. E. W. Bauer, S. T. B. Goennenwein, and E. Saitoh, Phys. Rev. Lett. **110**, 206601 (2013).
[7] S. Vélez, V. N. Golovach, A. Bedoya-Pinto, M. Isasa, E. Sagasta, M. Abadia, C. Rogero, L. E. Hueso, F. S. Bergeret, and F. Casanova, Phys. Rev. Lett. **116**, 016603 (2016).
[8] H. Wu, X. Zhang, C. H. Wan, B. S. Tao, L. Huang, W. J. Kong, and X. F. Han, Phys. Rev. B **94**, 174407 (2016).
[9] M. V. Costache, M. Sladkov, S. M. Watts, C. H. van der Wal, and B. J. van Wees, Phys. Rev. Lett. **97**, 216603 (2006).
[10] O. Mosendz, J. E. Pearson, F. Y. Fradin, G. E. W. Bauer, S. D. Bader, and A. Hoffmann, Phys. Rev. Lett. **104**, 046601 (2010).
[11] W. Zhang, W. Han, X. Jiang, S.-H. Yang, and S. S. P. Parkin, Nat. Phys. **11**, 496 (2015).
[12] L. Wang, R. J. H. Wesselink, Y. Liu, Z. Yuan, K. Xia, and P. J. Kelly, Phys. Rev. Lett. **116**, 196602 (2016).
[13] A. Hoffmann, IEEE Trans. Magn. **49**, 5172 (2013).
[14] G. Y. Guo, S. Murakami, T.-W. Chen, and N. Nagaosa, Phys. Rev. Lett. **100**, 096401 (2008).
[15] T. Tanaka, H. Kontani, M. Naito, T. Naito, D. S. Hirashima, K. Yamada, and J. Inoue, Phys. Rev. B **77**, 165117 (2008).
[16] J. Smit, Physica (Utrecht) **24**, 39 (1958).
[17] J. Smit, Physica (Utrecht) **21**, 877 (1955).
[18] L. Berger, Physica (Utrecht) **30**, 1141 (1964).
[19] L. Ma, H. A. Zhou, L. Wang, X. L. Fan, W. J. Fan, D. S. Xue, K. Xia, Z. Wang, R. Q. Wu, G. Y. Guo, L. Sun, X. Wang, X. M. Cheng, and S. M. Zhou, Adv. Electron. Mater. **2**, 1600112 (2016).
[20] R. Arias and D. L. Mills, Phys. Rev. B **60**, 7395 (1999).
[21] C. Burrowes, B. Heinrich, B. Kardasz, E. Montoya, E. Girt, Y. Y. Sun, Y. Y. Song, and M. Z. Wu, Appl. Phys. Lett. **100**, 092403 (2012).
[22] B. Heinrich, C. Burrowes, E. Montoya, B. Kardasz, E. Girt, Y. Y. Song, Y. Y. Sun, and M. Z. Wu, Phys. Rev. Lett. **107**, 066604 (2011).
[23] S. Dutta, K. Sankaran, K. Moors, G. Pourtois, S. Van Elshocht, J. Bömmels, W. Vandervorst, Z. Tőei, and C. Adelmann, J. Appl. Phys. **122**, 025107 (2017).
[24] Y. Tian, L. Ye, and X. F. Jin, Phys. Rev. Lett. **103**, 087206 (2009).
[25] L. F. Zhou, H. K. Song, K. Liu, Z. Z. Luan, P. Wang, L. Sun, S. W. Jiang, H. J. Xiang, Y. B. Chen, J. Du, H. F. Ding, K. Xia, J. Xiao, and D. Wu, Sci. Adv. **4**, eaao3318 (2018).
[26] L. Ma, L. L. Lang, J. Kim, Z. Yuan, R. Q. Wu, S. M. Zhou, and X. P. Qiu, Phys. Rev. B **98**, 224424 (2018).
[27] X. D. Tao, Q, Liu, B. F. Miao, R. Yu, Z. Feng, L. Sun, B. You, J. Du, K. Chen, S. Zhang, L. Zhang, Z. Yuan, D. Wu, and H. F. Ding, Sci. Adv. **4**, eaat1670 (2018).
[28] T. Lin, C. Tang, H. M. Alyahayaei, and J. Shi, Phys. Rev. Lett. **113**, 037203 (2014).

[29] H. L. Wang, C. H. Du, Y. Pu, R. Adur, P. C. Hammel, and F. Y. Yang, Phys. Rev. Lett. **112**, 197201 (2014).
[30] M. Weiler, M. Althammer, M. Schreier, J. Lotze, M. Pernpeintner, S. Meyer, H. Huebl, R. Gross, A. Kamra, J. Xiao, Y. T. Chen, H. J. Jiao, G. E. W. Bauer, and S. T. B. Goennenwein, Phys. Rev. Lett. **111**, 176601 (2013).
[31] M. Isasa, E. Villamor, L. E. Hueso, M. Gradhand, and F. Casanova, Phys. Rev. B **91**, 024402 (2015).
[32] M. I. Dyakonov and V. I. Perel, Phys. Lett. A **35**, 459 (1971).
[33] J. E. Hirsch, Phys. Rev. Lett. **83**, 1834 (1999).
[34] P. Scherrer, Nachr. Ges. Wiss. Göttingen, Math.-Phys. Kl. **1918**, 98 (1918).
[35] T. Valet and A. Fert, Phys. Rev. B **48**, 7099 (1993).
[36] R. J. Elliott, Phys. Rev. **96**, 266 (1954).
[37] Y. Yafet, J. Phys. Chem. Solids **21**, 99 (1961).
[38] J. Fabian and S. Das Sarma, J. Vac. Sci. Technol., B: Microelecton. Process. Phenom. **17**, 1708 (1999).
[39] M. I. D'yakonov and V. I. Perel', Fiz. Tverd. Tela **13**, 3581 (1971) [Sov. Phys. Solid State **13**, 3023 (1972)].
[40] M. D. Mower, G. Vignale, and I. V. Tokatly, Phys. Rev. B **83**, 155205 (2011).
[41] J. Ryu, M. Kohda, and J. Nitta, Phys. Rev. Lett. **116**, 256802 (2016).
[42] S. Geprägs, S. Meyer, S. Altmannshofer, M. Opel, F. Wilhelm, A. Rogalev, R. Gross, and S. T. B. Goennenwein, Appl. Phys. Lett. **101**, 262407 (2012).
[43] T. Kuschel, C. Klewe, J. M. Schmalhorst, F. Bertram, O. Kuschel, T. Schemme, J. Wollschläger, S. Francoual, J. Strempfer, A. Gupta, M. Meinert, G. Götz, D. Meier, and G. Reiss, Phys. Rev. Lett. **115**, 097401 (2015).
[44] M. Obstbaum, M. Decker, A. K. Greitner, M. Haertinger, T. N. G. Meier, M. Kronseder, K. Chadova, S. Wimmer, D. Ködderitzsch, H. Ebert, and C. H. Back, Phys. Rev. Lett. **117**, 167204 (2016).
[45] L. K. Zou, S. H. Wang, Y. Zhang, J. R. Sun, J. W. Cai, and S. S. Kang, Phys. Rev. B **93**, 014422 (2016).
[46] X. Zhou, M. Tang, X. L. Fan, X. P. Qiu, and S. M. Zhou, Phys. Rev. B **94**, 144427 (2016).
[47] L. L. Lang, S. M. Zhou, and X. P. Qiu, J. Phys. D: Appl. Phys. **52**, 085001 (2019).